From $Ag_2Sb_2O_6$ to $Cd_2Sb_2O_7$: Investigations on an anion-deficient to ideal pyrochlore solid solution

Citation	Laurita, G., Vielma, J., Winter, F., Berthelot, R., Largeteau, A., Pöttgen, R., . . . Subramanian, M. A. (2014). From $Ag_2Sb_2O_6$ to $Cd_2Sb_2O_7$: Investigations on an anion-deficient to ideal pyrochlore solid solution. Journal of Solid State Chemistry, 210(1), 65-73. doi:10.1016/j.jssc.2013.11.007
DOI	10.1016/j.jssc.2013.11.007
Publisher	Elsevier
Version	Accepted Manuscript
Citable Link	http://hdl.handle.net/1957/48746
Terms of Use	http://cdss.library.oregonstate.edu/sa-termsofuse

From $Ag_2Sb_2O_6$ to $Cd_2Sb_2O_7$: investigations on an anion-deficient to ideal pyrochlore solid solution

Geneva Laurita[a], Jason Vielma[b], Florian Winter[c], Romain Berthelot[a,d], Alain Largeteau[d], Rainer Pöttgen[c], G. Schneider[b], M. A. Subramanian[a]*

[a]*Department of Chemistry, Oregon State University, Corvallis, OR 97331, USA*

[b]*Department of Physics, Oregon State University, Corvallis, OR 97331, USA*

[c]*Institut für Anorganische und Analytische Chemie, Universität Münster, Corrensstrasse 30, D-48149 Münster, Germany*

[d]*CNRS, Univ. Bordeaux, ICMCB, UPR9048, F-33600 Pessac, France*

*Corresponding author: mas.subramanian@oregonstate.edu

Abstract:

A complete solid solution between the anion-deficient pyrochlore $Ag_2Sb_2O_6$ and the ideal pyrochlore $Cd_2Sb_2O_7$ has been synthesized through the standard solid state ceramic method. Each composition has been characterized by various different techniques, including powder X-ray diffraction, optical spectroscopy, electron paramagnetic resonance and ^{121}Sb Mössbauer spectroscopy. Computational methods based on density functional theory complement this investigation. Photocatalytic activity has been studied, and transport properties have been measured on pellets densified by spark plasma sintering. The analysis of the data collected from these various techniques enables a comprehensive characterization of the complete solid solution and revealed an anomalous behavior in the Cd-rich end of the solid solution, which has been proposed to arise from a possible radical O^- species in small concentrations.

Keywords: $Ag_2Sb_2O_6$, $Cd_2Sb_2O_7$, pyrochlore, optical properties, thermogravimetric analysis, ^{121}Sb Mössbauer spectroscopy

1. Introduction:

The compound $Ag_2Sb_2O_6$ (commonly referred to as $AgSbO_3$) was first reported in 1938, and structurally characterized as a defect pyrochlore in 1969.[1,2] This anion-deficient pyrochlore is a material of interest due to its observed photocatalytic activity when irradiated with visible light.[3] This visible-light response is facilitated by a narrow band gap of approximately 2.6 eV.[3,4] Detailed DFT calculations[3–5] show that the narrow band gap is a result of the orbital compositions at the valence band maxima (VBM) and the conduction band minima (CBM). The VBM is composed of primarily Ag 4*d* and O 2*s* orbitals, and the orbital interaction results in an elevation in the energy of the VBM. The CBM is composed of diffuse Ag 5*s* and Sb 5*s*-O 2*p* orbitals. The combination of the elevated VBM energy and the diffuse 5*s* orbitals at the CBM provide this material with a narrow band gap that utilizes the visible portion of the light spectrum for photocatalytic reactions.

From a properties view, a relatively low thermal conductivity of 0.824 $Wm^{-1}K^{-1}$ for $Ag_2Sb_2O_6$ has been reported, and the thermoelectric properties were characterized with a low thermoelectric Figure-of-Merit, ZT, of 0.06 at 873 K.[6] $Ag_2Sb_2O_6$ has also been studied to show it is an n-type mixed ionic and electronic conductor,[7] exhibiting a conductivity of approximately $10^{-1}\Omega^{-1}cm^{-1}$ in thin film form.[8]

$Cd_2Sb_2O_7$ was first reported in 1945, and has been structurally characterized and determined to adopt the pyrochlore structure.[9–11] A study on the electrical conductivity of sintered samples determined $Cd_2Sb_2O_7$ to be an n-type semiconductor.[12] There have not been any previous reports on the electronic properties of $Cd_2Sb_2O_7$.

Both $Ag_2Sb_2O_6$ and $Cd_2Sb_2O_7$ crystallize in the pyrochlore structure with similar covalency, lattice, and synthesis parameters. The primary difference is that $Ag_2Sb_2O_6$ forms an anion-deficient pyrochlore, whereas $Cd_2Sb_2O_7$ forms the ideal pyrochlore structure. The ideal pyrochlore structure is often described

as two three-dimensional interpenetrating networks of corner-sharing $BO_{6/2}$ octahedra and A_2O chains in the channels of the polyhedral framework.[13] This cubic structure is described symmetrically by the space group $Fd\bar{3}m$, and is often represented with the formula $A_2B_2O_7$. The pyrochlore formula $A_2B_2O_7$ can also be written $A_2B_2O_6O'$ due to the fact that oxygen is found on two distinct sites: on the corners of the BO_6 octahedra (48*f* site), and in the A_2O' (8*b* site) chain.[14] In the anion-deficient pyrochlore structure, there is only one type of oxygen ion, located exclusively on the corners of the BO_6 octahedra. Therefore, the O' ions are not present, leading to the formula $A_2B_2O_6$, (often shortened to ABO_3). A comparison between the full and anion-deficient pyrochlore structures is shown in Figure 1.

Although a partial solid solution $(Cd_{1-x}Ag_x)Sb_2O_{6.8}$ (x= 0.00, 0.05, 0.10, and 0.15) has been studied as a potential alcohol gas-sensing material, including a study of the observed conductivities in the solution,[15] to the best of our knowledge there is no report of a full solid solution between $Ag_2Sb_2O_6$ and $Cd_2Sb_2O_7$. For these reasons, the compositions between $Ag_2Sb_2O_6$ and $Cd_2Sb_2O_7$ were investigated in an attempt to tune the band structure and the properties of $Ag_2Sb_2O_6$ by changing the orbital overlap between the Ag 4*d* and O 2*p* orbitals. As the solid solution progresses, a transition between the anion-deficient to ideal pyrochlore is expected, accompanied by an increase in the oxygen content within the unit cell. This paper presents the first report of the full solid solution between the anion-deficient pyrochlore $Ag_2Sb_2O_6$ and the ideal pyrochlore $Cd_2Sb_2O_7$, and aims to qualitatively study the solid solution through X-ray diffraction (XRD), thermogravimetric analysis, density functional theory, diffuse reflectance optical properties, transport properties (on samples densified by spark plasma sintering), electron paramagnetic resonance and ^{121}Sb Mossbauer spectroscopy.

2. Experimental:

Polycrystalline samples were prepared by thoroughly grinding stoichiometric amounts of Ag_2O (Aldrich, 99+%) or Ag metal (Alfa Aesar, 325 mesh, 99.9%), CdO (Sigma Aldrich 99.99+%), and Sb_2O_3 (J. T. Baker Analyzed Reagent) in an agate mortar and pestle with acetone. The samples were then pelletized and annealed in air at 900 °C for 24-48 hours in an alumina boat with intermediate grindings.

Powders were first characterized through XRD with a Rigaku Miniflex II diffractometer using Cu Kα radiation and a graphite monochromator. Powder samples were loaded onto a "zero background" oriented Silicon single crystal sample holder (MTI corp.) to maximize the detection of minor impurity phases. Data was collected from 10-120 ° 2θ with a step size of 0.02 ° 2θ and a dwell time of 2.0 s. Room temperature lattice parameters were refined through the Le Bail method[16] using the GSAS software and EXPGUI user interface. [17,18]

The mass variation during the synthesis of the compounds was studied through thermogravimetric analysis (TGA) using a Metler Toledo TGA 850. Powdered starting materials were loaded in an alumina crucible and heated under O_2 flow to 900°C, with a ramp rate of 5°C/minute.

Optical spectra were determined by collecting the diffuse reflectance of the powders in the region of 200-1100 nm, using a halogen lamp source passed through a bifurcated optical fiber. The diffuse light reflected by the powders was collected with the optic cable and taken to an Ocean Optics HR4000 spectrophotometer. MgO (99.5%, Cerac) was used as a white reference. The collected data were converted to absorbance using the Kubelka-Munk equation.[19]

All density functional theory (DFT) calculations used the projector augmented plane wave method[20,21] as implemented in the Vienna *ab-initio* simulation package (VASP)[22,23] together with two different approximations for the exchange-correlation functional: the Perdew-Burker-Ernzerhoff (PBE)[24] generalized gradient approximation and the Heyd, Scuzeria, and Ernzerhoff (HSE06) hybrid functional[25,26]. It has been shown that using HSE06 for $Ag_2Sb_2O_6$ resulted in lattice constants, volume, bond lengths, and a band gap much closer to experimentally determined parameters[5]. Additional

calculation parameters include a 500 eV plane-wave cutoff (400 eV for HSE06), using Fermi-smearing with a width of 0.05 eV, and a gamma-centered 6 x 6 x 6 k-point grid.

Sample densification was done with spark plasma sintering (SPS) (DR. SINTER LAB Spark Plasma Sintering system, Model SPS-515S) at sintering temperature of 850°C for dwell time of 5 minutes in vacuum (8 Pa) under 50 MPa of pressure which was applied at the start of sintering cycle. The constant heating and cooling rate of 100^{o}C/min was employed for all the experiments with 2 g of powder inside graphite mold of 10 mm inner diameter. The temperature inside the graphite mold was controlled with pyrometer. Residual graphite from the SPS process was removed from the sample by mechanical sanding of the pellets and verification of phase purity through XRD.

High temperature (30-800°C) resistivity and Seebeck measurements were performed on densified samples with an ULVAC-RIKO ZEM 3 under a static helium atmosphere.

The photocatalytic activity was analyzed with a reactor setup in conjunction with UV-Vis spectroscopy. The reactor flask was a quartz round-bottom flask with one optically flat side to allow for minimal reflection of the incoming beam of light, and was housed in a dark box to exclude ambient light from the reaction. Approximately 0.0200 g of each powdered sample was suspended in a 2.0x10^{-5} M solution of methylene blue and stirred in a dark box for two hours to allow for adsorption of the dye onto to the surface of the sample. The reactor was then irradiated with light from a 300 W Xenon lamp source (Newport Corp.) under constant stirring. The intensity of the lamp was regulated with a Thorlabs PM100USB power and energy meter outfitted with a SC103C thermal power sensor. The power output was kept constant at 155 mW at the reactor face for all samples. Sample aliquots were withdrawn every 10-15 minutes followed by centrifugation to remove the powdered samples from the solution. The solution was then analyzed with an Ocean Optics ISS-UV-Vis spectrometer to determine the maximum absorption of the methylene blue.

A $Ba^{121}SnO_3$ source was used for the Mössbauer spectroscopic experiments and the quoted values of the isomer shifts are given relative to this material. The measurements were carried out in the usual transmission geometry at 78 K. The temperature was controlled by a resistance thermometer (±0.5 K accuracy) and the Mössbauer source was kept at room temperature. The samples were enclosed in small PMMA containers at a thickness corresponding to about 10 mg Sb/cm^2. The total counting time was approximately 3 days per spectrum. Fitting of the spectra was performed with the NORMOS-90 program system.[27]

3. Results and Discussion:

3.1 Structural Characterization:

XRD patterns obtained for the nominal series $(Ag_{1-x}Cd_x)_2Sb_2O_{6+x}$, x= 0.0, 0.2, 0.4, 0.6, 0.8 and 1.0 are shown in Figure 2 and evidence a complete solid solution. Indeed all diffraction peaks can be indexed to a cubic lattice with the $Fd\bar{3}m$ space group, indicating the pyrochlore structure is retained through the series. The peak shape indicates the samples are highly crystalline, and the background of the patterns shows no evidence of the presence an amorphous phase. Le Bail analysis of the patterns shows that the lattice parameter remains relatively unchanged throughout the solid solution, as is expected based on the reported unit cell dimensions of the end members. However, it does seem surprising that as the smaller cadmium cation is substituted for the larger silver cation, the lattice parameter does not change. Therefore, there must be a compensating factor to account for the observed trend in the lattice parameter evolution. As the solution progresses from anion-deficient pyrochlore $Ag_2Sb_2O_6$ to the ideal pyrochlore $Cd_2Sb_2O_7$, the oxygen content in the unit cell increases according to the formula $(Ag_{1-x}Cd_x)_2Sb_2O_{6+x}$, as shown in the following section. Consequently, the unchanging lattice parameter evolution is a result of the two counterbalancing processes: the substitution of a smaller cation (cadmium) into the lattice, accompanied by an increase in the number of atoms in the unit cell (addition of oxygen).

3.2 Thermogravimetric Analysis:

Analysis through XRD reveals that a solid solution between silver and cadmium is obtained with the pyrochlore structure. However, as stated in the introduction, $Ag_2Sb_2O_6$ is an anion-deficient pyrochlore, whereas $Cd_2Sb_2O_7$ is an ideal pyrochlore. It can be assumed that the oxygen content as the series progresses from anion-deficient to ideal is variable. Quantification of the oxygen content using XRD is unfavorable due to the low scattering factor of oxygen. Neutron diffraction is unfavorable as well due to the high absorption cross section of cadmium (2520 barn).[28] Therefore, alternative methods must be employed to gain insight into the amount of oxygen in each particular composition in the solution. One way to analyze the oxygen composition is by monitoring the mass gain during the synthesis reaction.

The reactions for $Ag_2Sb_2O_6$, from either Ag_2O or Ag metal, and $Cd_2Sb_2O_7$ are as follows:

$$Ag_2O + Sb_2O_3 + O_2 \rightarrow Ag_2Sb_2O_6 \qquad (1)$$

$$2Ag + Sb_2O_3 + \frac{3}{2}O_2 \rightarrow Ag_2Sb_2O_6 \qquad (2)$$

$$2CdO + Sb_2O_3 + O_2 \rightarrow Cd_2Sb_2O_7 \qquad (3)$$

For the cadmium end-member, there is a total theoretical mass gain of 5.83%. For the silver end-member, there is a theoretical mass gain of 6.12% with a precursor of Ag_2O (equation 1) or 9.46% with a precursor of Ag (equation 2). Therefore, the use of Ag metal as a silver precursor is preferred as it allows a greater differentiation between the mass change of the two end members. Figure 3 shows the TGA curves obtained for varying cadmium content with the use of Ag metal as the silver precursor. All curves exhibit two distinct increases in mass, indicating that the pyrochlore formation is a two-step process. The first mass gain around 550 °C represents a mass increase between 2 to 2.5%, and is uniform and very rapid in all curves. The second mass gain is more gradual as a function of temperature (between 650 and 900 °C). It exhibits a large variation from the cadmium-rich end (approximately a 6% total gain

for $Cd_2Sb_2O_7$) to the silver-rich end (up to approximately a 10% total increase for $Ag_2Sb_2O_6$). XRD analysis after the TGA runs confirms that the pyrochlore phase is formed in each case.

According to the two distinct mass gains, the two step process during the pyrochlore formation of the pyrochlore compounds can be hypothesized as the following: between 500-550 °C, half of the Sb^{3+} is oxidized to Sb^{5+}, resulting in the formation of Sb_2O_4 and a theoretical weight gain of 3.20%. Further TGA experiments stopped after this first gain, coupled with XRD analysis confirms the presence of Sb_2O_4, while Ag metal is still unchanged. The second mass gain between 600-900 °C is the formation of the pyrochlore phase, with a simultaneous oxidation of the remaining Sb^{3+} to Sb^{5+} and Ag^0 to Ag^+. This represents the additional theoretical weight gain of 6.26% for $Ag_2Sb_2O_6$ and 2.36% for $Cd_2Sb_2O_7$ (only Sb oxidation). Using TGA, it appears to be impossible to differentiate the oxidation of Ag metal with the oxidation of the second half of Sb^{3+}, as they occur in the same temperature range.

The summarized mass gain as compared to the theoretical value is shown in Figure 4. It appears that there is a linear mass gain in the silver-rich end of the series, suggesting that in this region the oxygen content strictly follows that of the cadmium. Therefore, the general synthesis equation can be modeled linearly as

$$2(1\text{-}x)Ag + (2x)CdO + Sb_2O_3 \xrightarrow{O_2} (Ag_{1-x})_2(Cd_x)_2Sb_2O_{6+x} \qquad (4)$$

3.3 Optical Characterization:

It was noticed that the increase in cadmium content was accompanied by a color change from yellow ($Ag_2Sb_2O_6$) to violet/grey ($Ag_{0.4}Cd_{0.8}Sb_2O_{6+\delta}$) to tan ($Cd_2Sb_2O_7$). This observation prompted the collection of optical data on the series to analyze the apparently changing band gap (Figure 5). Grain size calculations (from the Scherrer[29] equation and Williamson-Hall[30] plot) reveal particle sizes within

the same order of magnitude (200-600 nm), suggesting that the observed color progression is not a result of the particle size, but of the changing band structure. After transforming the collected data using the Kebulka-Munk equation, the band gap was estimated by extrapolating the linear portion of the absorption onset to the x-axis in a plot of absorption versus energy, following the work of Mizoguchi *et al*.[4] Table 1 shows the estimated band gaps, as well as a comparison to the band gaps for $Ag_2Sb_2O_6$ and $Cd_2Sb_2O_7$ from the literature.[4] An increasing band gap as the series progresses from $Ag_2Sb_2O_6$ to $Cd_2Sb_2O_7$ is experimentally observed. Upon further analysis, it is noted that at an approximate nominal composition of $AgCdSb_2O_{6.5}$, an additional absorption band emerges and is observed until a nominal composition of $Cd_2Sb_2O_7$.

3.4 Computational Results:

The equilibrium lattice parameters for $Ag_2Sb_2O_6$ and $Cd_2Sb_2O_7$ using DFT with HSE06 are 10.22 Å and 10.23 Å, respetively, which are very close to both the experimental equilibrium lattice constants of 10.25 Å. DFT with PBE give equilibrium lattice constants of 10.43 Å and 10.44 Å for $Ag_2Sb_2O_6$ and $Cd_2Sb_2O_7$, respectively. Figure 6 gives the band structure diagrams of both compounds. DFT with HSE06 gives band gaps of 2.26 eV for $Ag_2Sb_2O_6$ and 2.50 eV for $Cd_2Sb_2O_7$. DFT/PBE portray $Ag_2Sb_2O_6$ as being a metal and $Cd_2Sb_2O_7$ with a band gap of 0.39 eV. When using DFT with HSE06, the bottom of the conduction band is shifted up greatly in both compounds, while the rest of the valence bands are only shifted slightly from literature DFT with PBE calculations. [5] Figure 7 gives the total and partial density of states (DOS) for both compounds. For $Ag_2Sb_2O_6$, the valence band maximum is dominated by Ag 4*d* and O 2*p* states, and the conduction band minimum is composed of Sb 5*s* and O 2*p* states, in agreement with Allen *et al*. [5] For $Cd_2Sb_2O_7$, the conduction band minimum is also composed of Sb 5*s* and O 2*p* states, but the valence band maximum is primarily made of O 2*p* states. The top of the Cd 4*d* states are located 6 eV below the valence band maximum. The orbital contributions at the VBM of $Cd_2Sb_2O_7$ have been further analyzed

by calculating the partial contributions to the DOS near the Fermi level of the two types of oxygen atoms (48*f* and 8*b*). By comparing the partial DOS (Figure 8), it can be seen that the orbitals closest to the Fermi level originate from the O' oxygen in the 8*b* site. The absence of these partials from the DOS of $Ag_2Sb_2O_6$ indicates that it is indeed the O' oxygen that is being acquired as the series progresses from $Ag_2Sb_2O_6$ to $Cd_2Sb_2O_7$.

3.5 Transport Properties:

Obtaining high-density samples seems to be very difficult, in agreement with the literature in the case of $Ag_2Sb_2O_6$.[6] Samples prepared through conventional solid state routes yields densities of only 50% of that of the theoretical values.[4] To increase the density of the samples, Spark Plasma Sintering (SPS) was applied to the samples. Densification was variable by composition, and at longer sintering time, higher temperature, and higher pressures, decomposition of the samples was evident. However, phase pure samples were obtained through SPS, and a summary of the increased densities can be seen in Table 2. The highest densities observed after sintering were between 70-75% of the theoretical values. High temperature resistivity and Seebeck measurements indicate that as the cadmium content increases, the samples retain n-type conductivity accompanied by an increase in the measured resistivity (Figure 9). This follows the expected trend based on the electronic properties of the parent compounds $Ag_2Sb_2O_6$ and $Cd_2Sb_2O_7$.

3.6 Photocatalytic Activity:

The photocatalytic activity was evaluated with the described apparatus for a total irradiation time of 2 hours, with the maximum absorption of methylene blue evaluated at ten minute intervals. The maximum absorption was plotted as a function of time, and compared against a blank (no sample in reactor flask) and a Degussa P25 TiO_2 standard. The value for the degradation amount from the blank

was subtracted from each run to obtain the final degradation percentage of the methylene blue after 2 hours irradiation time. The normalized data for each sample along the series is shown in Figure 10. It is observed that the total amount of methylene blue degraded by the sample decreases with increasing cadmium content along the series. Based on an estimation of the band gap, it was determined that an increase in the magnitude was observed with an increase in cadmium content. It was previously hypothesized that a change in the magnitude of the band gap could be induced by changing the amount of orbital overlap between the Ag 4*d* and O 2*p* orbitals, or in other words, by changing the Ag-O bond length. Throughout the series, it was indicated that the change in lattice parameter was minimal, and it is speculated that the change in the Ag-O bond length will be minimal as well. Therefore, the evolution of the band gap throughout the series must be attributed elsewhere. Detailed DOS calculations (Figures 6-8) show that as the cadmium content increases, the VBM becomes no longer dominated by Ag 4*d*-O 2*p* orbitals, but instead becomes dominated by primarily oxygen orbitals. This effectively lowers the energy of the VBM, resulting in the observed increase in the magnitude of the band gap.

Along with the increase in the magnitude of the band gap, an increase in the resistivities of the samples was observed as the cadmium content increased. Both of these properties play a large role in the photocatalytic activity of a material, and it is observed that a decrease in the activity of the samples follows the increase in the cadmium content as well. This decrease is primarily attributed to the increasing resistivity, which can also be attributed to the increase in the magnitude of the band gap. While an enhancement of the photocatalytic activity was not observed, this work illustrates the dependence of this activity not only on the magnitude of the band gap, but on the orbital composition in the VBM and CBM.

3.7 Investigation of the Cadmium-Rich End of the Solid Solution:

As the series progresses from $Ag_2Sb_2O_6$ to $Cd_2Sb_2O_7$, it is expected that a linear gain of oxygen would be observed as cadmium content increases. This hypothesis can be modeled by the formula $(Ag_{1-x}Cd_x)_2Sb_2O_{6+x}$. However, rationalizing this linear relationship near the cadmium-rich end presents a problem. As previously mentioned, the ideal pyrochlore structure can be described as two interpenetrating networks: a network of BO_6 octahedra, and a network of A_2O chains. For $Cd_2Sb_2O_7$, this would be equivalent to a network of SbO_6 polyhedra and a network of Cd_2O chains. This Cd_2O chain consists of strong bonds between the alternating cadmium and oxygen atoms. As silver is introduced into this system, the SbO_6 polyhedra remain unchanged, but the silver will replace a cadmium atom on the Cd_2O chain. After this substitution, based on a linear oxygen-cadmium relationship, the A_2O chain would now consist of neighboring cadmiums that are bonded to only one oxygen atom. This creates an unfavorable situation of severely under-bonded cadmium cations in the compound, which could be alleviated by distributing charge elsewhere. Three alternative models were proposed for the cadmium-rich end of the solid solution:

1. The formation of Ag^{2+}:

$$2(1-x)CdO + (2x)Ag + Sb_2O_3 \xrightarrow{O_2} (Cd^{2+}_{1-x}Ag^{2+}_{x})_2Sb_2O_7 \qquad (6)$$

2. An e^- trapped in an O^{2-} vacancy, creating a color center:

$$2(1-x)CdO + (2x)Ag + Sb_2O_3 \xrightarrow{O_2} Cd^{2+}_{2-x}Ag^{+}_{x}Sb_2O_{7-x}e^-_x \qquad (7)$$

$$2(1-x)CdO + (2x)Ag + Sb_2O_3 \xrightarrow{O_2} Cd^{2+}_{2-x}Ag^{+}_{x}Sb_2O_{7-x} \qquad (8)$$

3. A hole color center trapped on an interstitial oxygen, essentially creating an O^- species:

$$2(1-x)CdO + (2x)Ag + Sb_2O_3 \xrightarrow{O_2} Cd^{2+}_{2-x}Ag^{+}_{x}Sb_2O_{7-x}O^-_x \qquad (9)$$

$$2(1\text{-}x)CdO + (2x)Ag + Sb_2O_3 \xrightarrow{O_2} Cd^{2+}_{2-x}Ag^{+}_{x}Sb_2O_7 \qquad (10)$$

Electron Paramagnetic Resonance (EPR) spectra collected at Roosevelt University of the cadmium-rich samples did not show evidence for the presence of Ag^{2+}, as there is no hyperfine splitting present (Supplemental Figure S1).[31] To further investigate the origin of the EPR signal, it was necessary to exclude other possible sources.

In the solid solution, another possible source for an EPR signal could arise from antimony in the system that is not in the pentavalent oxidation state. One possibility is that if an electron color center is generated, it could become trapped on antimony, creating Sb^{4+}. However, due to the tendency towards disproportionation to Sb^{3+} and Sb^{5+}, this is unlikely. Another possibility is the presence of Sb^{3+} on the A-site of the pyrochlore structure, which has been reported in the literature.[32–37] Therefore, it was necessary to employ ^{121}Sb Mössbauer spectroscopy to determine the oxidation and coordination of antimony throughout the series. The well-resolved ^{121}Sb Mössbauer spectra of the pyrochlores $Ag_2Sb_2O_6$, $AgCdSb_2O_{6+x}$, $Ag_{0.4}Cd_{1.6}Sb_2O_{6+x}$, and $Cd_2Sb_2O_7$ are presented in Figure 11 together with transmission integral fits. The corresponding fitting parameters are listed in Table 3. All spectra show single signals with isomer shifts ranging from 0.48 mm/s ($Cd_2Sb_2O_7$) to 0.58 mm/s ($Ag_2Sb_2O_6$) which are indicative for purely pentavalent antimony**.**[38] The slightly smaller isomer shift of the cadmium compound indicates slightly smaller 5*s* electron density at the antimony nuclei. Since the antimony atoms have cubic site symmetry $Fd\bar{3}m$, the spectra show no electric quadrupole splitting. The experimental line width parameters are all similar within the combined standard deviations and similar to many other antimony oxides and antimony intermetallics. [39–43] The spectra were recorded over the broad range of ±25 mm/s. No signals are evident around –15 mm/s, indicating stable pentavalent antimony in all samples.

As no Ag^{2+}, Sb^{4+}, or Sb^{3+} is present in the sample, it is concluded that the EPR signal is arising from a radical species present in relatively low concentrations, such as an O^- species. Further discussion on EPR can be found in Supporting Information.

The evolution of a broad absorption band in the cadmium rich samples, combined with an observation of a smoky color, also suggests that there may be the evolution of another species in the samples. It has been shown that the smoky color in smoky quartz is a result of hole color centers in the system.[44,45] In the SiO_2 network of smoky quartz, a Si^{+4} atom is replaced with an Al^{+3} atom, generating a hole. This generated hole becomes trapped on a nearby interstitial O^{2-}, effectively creating an O^-. A similar mechanism may be responsible for the observed optical properties and EPR spectra of the $Ag_2Sb_2O_6$-$Cd_2Sb_2O_7$ solid solution.

4. Conclusions:

A complete solid solution between $Ag_2Sb_2O_6$ and $Cd_2Sb_2O_7$ was synthesized and characterized to investigate the effect of substitution upon the observed properties of the visible-light photocatalyst $Ag_2Sb_2O_6$. Substitution of cadmium resulted in a simultaneous increase in the optical band gap and decrease in the resistivity of the samples, which are attributed to the observed decrease in the degradation rate of methylene blue upon irradiation with light. Anomalous behavior was observed in the optical data of the cadmium-rich samples, and further investigation with EPR and ^{121}Sb Mössbauer spectroscopy indicate that neither Ag^{2+} or Sb^{3+} are present. Therefore, the observed behavior of the cadmium-rich samples is attributed to a small concentration of radical species such as O^- in the samples, which is proposed to arise from a hole color center formed in the samples. Through cation substitution,

the properties of $Ag_2Sb_2O_6$ were successfully manipulated and, in combination with theoretical results, give insight to the origin of the observed photocatalytic activity of this material of interest.

Acknowledgement

This work was supported by NSF grant DMR 0804167. We thank Dr. Arthur Sleight for his helpful discussions in regards to the anomalous behavior observed in the cadmium-rich samples, and Dr. Joshua Telser at Roosevelt University for collecting the EPR spectra on the samples.

References:

[1] N. Schrewelius, Z. Anorg. Chem. 238 (1938) 241.

[2] A.W. Sleight, Mater. Res. Bull. 4 (1969) 377.

[3] T. Kako, N. Kikugawa, J. Ye, Catal. Today 131 (2008) 197.

[4] H. Mizoguchi, H.W. Eng, P.M. Woodward, Inorg. Chem. 43 (2004) 1667.

[5] J.P. Allen, M.K. Nilsson, D.O. Scanlon, G.W. Watson, Phys. Rev. B Condens. Matter 83 (2011) 035207.

[6] H.-Y. Sang, J.-F. Li, J. Alloys Compd. 493 (2010) 678.

[7] Y. Matsumoto, K. Funaki, J. Hombo, Y. Ogawa, J. Solid State Chem. 99 (1992) 336.

[8] M. Yasukawa, H. Hosono, N. Ueda, H. Kawazoe, Solid State Commun. 95 (1995) 399.

[9] A. Bystrom, B. Hok, B. Mason, Ark. Kemi, Mineral. Och Geol. 15B (1941) 8.

[10] J.-Y. Moisan, J. Pannetier, J. Lucas, C. R. Acad. Sci., Ser. IIc: Chim. 271 (1970) 402.

[11] F. Brisse, D.J. Stewart, V. Seidl, O. Knop, Can. J. Chem. 50 (1972) 3648.

[12] B.R. Li, J.L. Zhang, J. Mater. Sci. Lett. 9 (1990) 109.

[13] A.W. Sleight, Inorg. Chem. 7 (1968) 1704.

[14] M.A. Subramanian, G. Aravamudan, G.V. Subba Rao, Prog. Solid State Chem. 15 (1983) 55.

[15] Y.-F. Liu, X. Liu, J. Yu, Sens. Actuators, B 61 (1999) 208.

[16] A. Le Bail, Powder Diffr. 20 (2005) 316.

[17] A.C. Larson, R.B. Von Dreele, Los Alamos Nat. Lab. Rep. LAUR (1994) 89.

[18] B.H. Toby, J. Appl. Crystallogr. 34 (2001) 210.

[19] P. Kubelka, F. Munk, Zeitschrift Für Tech. Phys. 12 (1931) 593.

[20] P.E. Blochl, Phys. Rev. B 50 (1994) 17953.

[21] G. Kresse, D. Joubert, Phys. Rev. B 59 (1999) 1758.

[22] G. Kresse, J. Hafner, Phys. Rev. B 49 (1994) 14251.

[23] G. Kresse, J. Furthmuller, Phys. Rev. B 54 (1996) 11169.

[24] J.P. Perdew, K. Burke, M. Ernzerhoff, Phys. Rev. Lett. 77 (1996) 3865.

[25] S. Heyd, G.E. Scuseria, M. Ernzerhoff, J. Chem. Phys. 118 (2003) 8207.

[26] A. V. Krukau, O.A. Vydrov, A.F. Izmaylov, G.E. Scuseria, J. Chem. Phys. 125 (2006) 224106.

[27] R. A. Brand, NORMOS Mössbauer Fitting Program, Universitat Duisburg, Duisburg, Germany, 2007.

[28] A. Munter, NIST Center for Neutron Research Neutron Scattering Lengths and Cross Sections, Http://www.ncnr.nist.gov/resources/n-Lengths/, 2011.

[29] A. Patterson, Phys. Rev. 56 (1939) 978.

[30] G. Williamson, W. Hall, Acta Met. 1 (1953) 22.

[31] J. Telser, Personal Communication (2012).

[32] M. Bouchama, M. Tournoux, Rev. Chim. Miner. 12 (1975) 93.

[33] M. Bouchama, M. Tournoux, Rev. Chim. Miner. 12 (1975) 80.

[34] P.Y. Piffard, M. Tournoux, Acta Crystallogr. Sect. B Struct. Crystallogr. Cryst. Chem. B35 (1979) 1450.

[35] P.Y. Piffard, M. Dion, M. Tournoux, Acta Crystallogr. Sect. B Struct. Crystallogr. Cryst. Chem. B34 (1978) 366.

[36] D.J. Stewart, O. Knop, Can. J. Chem. 48 (1970) 1323.

[37] W.S. Brower, D.B. Minor, H.S. Parker, R.S. Roth, J.L. Waring, Mater. Res. Bull. 9 (1974) 1045.

[38] P.E. Lippens, Solid State Commun. 113 (2000) 399.

[39] T. Birchall, B. Della Valle, Chem. Commun. (1970) 675.

[40] J.B. Wooten, G.G. Long, L.H. Bowen, J. Inorg. Nucl. Chem. 36 (1974) 2177.

[41] Y.M. Jansen, J. Pebler, K. Dehnicke, Zeitschrift Für Anorg. Und Allg. Chemie 495 (1982) 120.

[42] R. Mishra, R. Pottgen, R.-D. Hoffmann, T. Fickenscher, M. Eschen, H. Trill, B.D. Mosel, Z. Naturforsch. B Chem. Sci. 57 (2002) 1215.

[43] I. Schellenberg, T. Nigles, R. Pöttgen, Z. Naturforsch. B Chem. Sci. 63 (2008) 834.

[44] O.F. Schirmer, Solid State Commun. 18 (1976) 1349.

[45] R. Gillen, J. Robertson, Phys. Rev. B 85 (2012) 014117.

[46] K. Yanagawa, Y. Ohki, T. Omata, H. Hosono, N. Ueda, H. Kawazoe, Jpn. J. Appl. Phys. 33 (1994) L238.

Tables:

Table 1.

Compound	Estimated Main-Gap Band Gap (eV)
$Ag_2Sb_2O_6$	2.70
	2.7[4]
$(Ag_{0.9})_2(Cd_{0.1})_2Sb_2O_{6+\delta}$	2.69
$(Ag_{0.8})_2(Cd_{0.2})_2Sb_2O_{6+\delta}$	2.73
$(Ag_{0.7})_2(Cd_{0.3})_2Sb_2O_{6+\delta}$	2.91
$(Ag_{0.6})_2(Cd_{0.4})_2Sb_2O_{6+\delta}$	2.79
$(Ag_{0.5})_2(Cd_{0.5})_2Sb_2O_{6+\delta}$	2.90
$(Ag_{0.4})_2(Cd_{0.6})_2Sb_2O_{6+\delta}$	2.92
$(Ag_{0.3})_2(Cd_{0.7})_2Sb_2O_{6+\delta}$	2.94
$(Ag_{0.2})_2(Cd_{0.8})_2Sb_2O_{6+\delta}$	3.05
$(Ag_{0.1})_2(Cd_{0.9})_2Sb_2O_{6+\delta}$	3.09
$Cd_2Sb_2O_7$	3.16
	2.7[4]-3.0[46]

Table 2.

Cadmium Content $(Ag_{1-x}Cd_x)_2SbO_{6+\delta}$	Conventional Solid State Reaction		Spark Plasma Sintering	
	Density (g/cm^3)	% Theoretical (based off nominal composition)	Density (g/cm^3)	% Theoretical (based off nominal composition)
0 (Theoretical[4])	6.81	--	--	--
0	3.42	50.2	5.21	**76.5**
0.1	3.38	49.4	3.78	55.2
0.2	3.28	47.7	5.14	**74.8**
0.3	3.27	47.4	--	--
0.4	3.31	47.7	4.82	**69.5**
0.5	3.43	49.2	3.83	54.9
0.6	3.20	45.7	4.10	58.5
0.7	3.14	44.6	--	--
0.8	3.28	46.4	4.04	57.1
0.9	3.76	52.9	3.99	56.2
1.0	3.10	43.4	3.76	52.7
1.0 (Theoretical[4])	7.14	--	--	--

Table 3.

Compound	δ (mm s^{-1})	Γ (mm s^{-1})
$Ag_2Sb_2O_6$	0.58(2)	3.55(6)
$AgCdSb_2O_{6+x}$	0.53(2)	3.53(7)
$Ag_{0.4}Cd_{1.6}Sb_2O_{6+x}$	0.54(2)	3.71(6)
$Cd_2Sb_2O_7$	0.48(2)	3.62(6)

Table and Figure Captions:

Figure 1. The anion-deficient (left) and ideal (right) pyrochlore structure-types that are adopted by $Ag_2Sb_2O_6$ and $Cd_2Sb_2O_7$, respectively. The additional O' ion in $Cd_2Sb_2O_7$ is shown in red.

Figure 2. PXRD data collected on the nominal series $(Ag_{1-x}Cd_x)_2Sb_2O_{6+x}$ (top). Lattice parameter evolution of the series (bottom) reveals a relatively unchanging unit cell.

Figure 3. Thermogravimetric analysis of the nominal series $(Ag_{1-x})_2(Cd_x)_2Sb_2O_{6+x}$ indicating the weight gain as the samples are formed.

Figure 4. A summary of the theoretical and experimental overall mass gained during formation as a function of cadmium content in the series. A linear gain of oxygen as cadmium content increase is assumed for this model, with a deviation from linearity in the cadmium-rich end. Systematic instrumental error in the mass gain has been removed from the theoretical models to facilitate comparison.

Figure 5. Images of the powders (left) reveal a change in color as the nominal series $(Ag_{1-x})_2(Cd_x)_2Sb_2O_{6+x}$ progresses. Diffuse reflectance data transformed with the Kebulka-Munk equation (right) reveal a changing band gap accompanying the color change.

Figure 6: Band structure diagrams using DFT with HSE06 of the defect pyrochlore $Ag_2Sb_2O_6$ and the ideal pyrochlore $Cd_2Sb_2O_7$. Both diagrams are shifted down such that 0 eV coincides with the valence band maximum (dotted line).

Figure 7: Partial and Total Electronic Density of States (DOS) using DFT with HSE06 for $Ag_2Sb_2O_6$ (a) and $Cd_2Sb_2O_7$ (b). The total DOS is in black, the s-states in red, the p-states in green, and the d-states in blue. Top plot is the total DOS, and the bottom three are the partial DOS of each atom. Each partial DOS shows how much the y-axis is scaled. DOS are shifted to set the Fermi energy to 0 eV.

Figure 8: Partial DOS for the two types of oxygen atoms in $Cd_2Sb_2O_7$. It can be seen that the band closest to the Fermi level originates from the oxygen in the 8*b* site.

Figure 9. High temperature resistivity and Seebeck data collected on the samples with a density 70% or greater of that of the theoretical values.

Figure 10. Degradation of methylene blue over a two-hour irradiation period, monitored by the normalized maximum absorbance of the dye at various time intervals.

Figure 11. Experimental and simulated ^{121}Sb Mössbauer spectra of the Sb(V) pyrochlores $Ag_2Sb_2O_6$, $AgCdSb_2O_{6+\delta}$, $Ag_{0.4}Cd_{1.6}Sb_2O_{6+\delta}$, and $Cd_2Sb_2O_7$ at 78 K.

Table 1. Summary of the estimated band gaps of the samples.

Table 2. Summary of the densities of solid state and SPS-prepared samples.

Table 3. Fitting parameters of ^{121}Sb Mössbauer spectroscopic measurements of several Sb(V) pyrochlores at 78 K. δ = isomer shift and Γ = experimental line width.

Figures:

Figure 1.

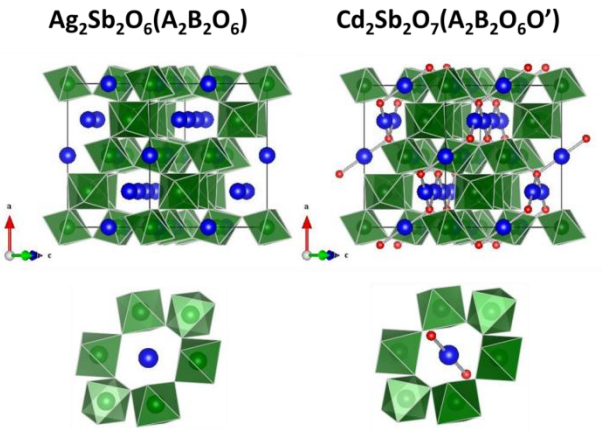

Figure 2.

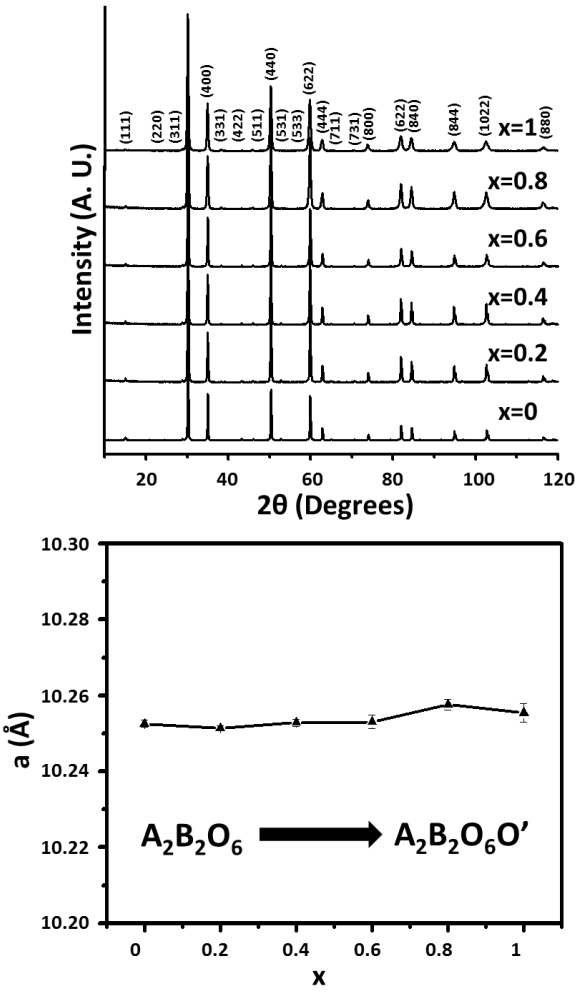
(111)
(220)
(311)
(400)
(331)
(422)
(511)
(440)
(531)
(533)
(622)
(444)
(711)
(731)
(800)
(622)
(840)
(844)
(1022)
(880)
x=1
x=0.8
x=0.6
x=0.4
x=0.2
x=0
Intensity (A. U.)
20
40
60
80
100
120
2θ (Degrees)
10.30
10.28
10.26
10.24
10.22
10.20
a (Å)
A2B2O6
A2B2O6O'
0
0.2
0.4
0.6
0.8
1
x

Figure 3.

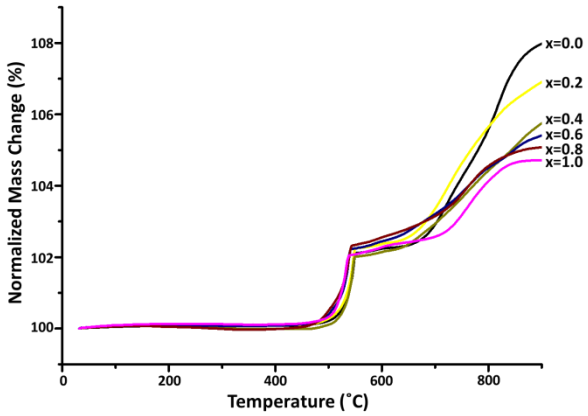
Normalized Mass Change (%)
108
106
104
102
100
0
200
400
600
800
Temperature (˚C)
x=0.0
x=0.2
x=0.4
x=0.6
x=0.8
x=1.0

Figure 4.

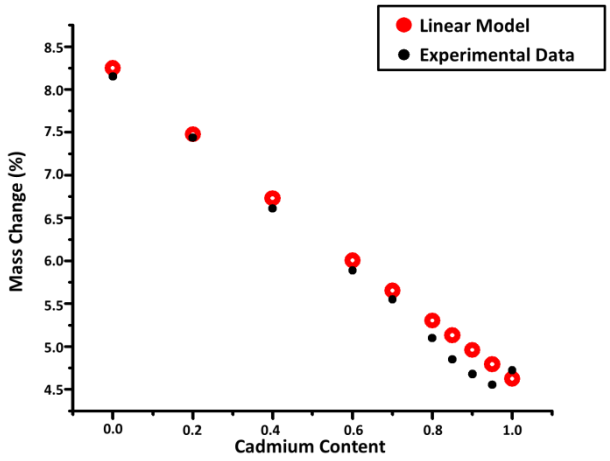
Linear Model
Experimental Data
Mass Change (%)
8.5
8.0
7.5
7.0
6.5
6.0
5.5
5.0
4.5
0.0
0.2
0.4
0.6
0.8
1.0
Cadmium Content

Figure 5.

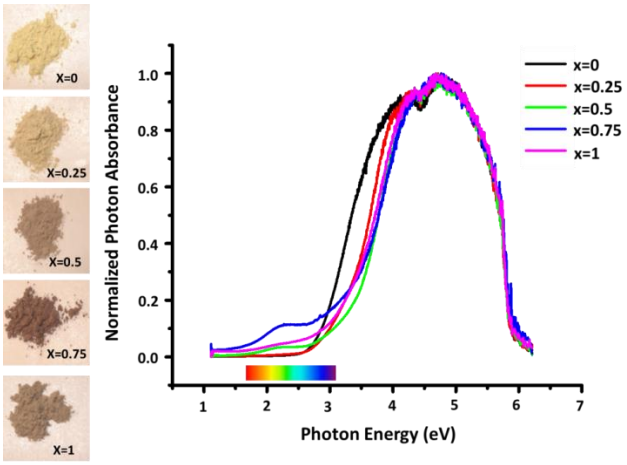
X=0
X=0.25
X=0.5
X=0.75
X=1
Normalized Photon Absorbance
1.0
0.8
0.6
0.4
0.2
0.0
1
2
3
4
5
6
7
Photon Energy (eV)
x=0
x=0.25
x=0.5
x=0.75
x=1

Figure 6:

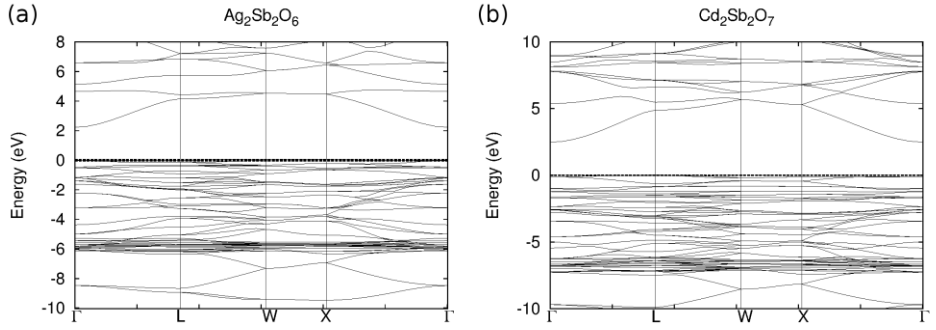
(a)
$Ag_2Sb_2O_6$
Energy (eV)
8
6
4
2
0
-2
-4
-6
-8
-10
Γ
L
W
X
Γ
(b)
$Cd_2Sb_2O_7$
Energy (eV)
10
5
0
-5
-10
Γ
L
W
X
Γ

Figure 7:

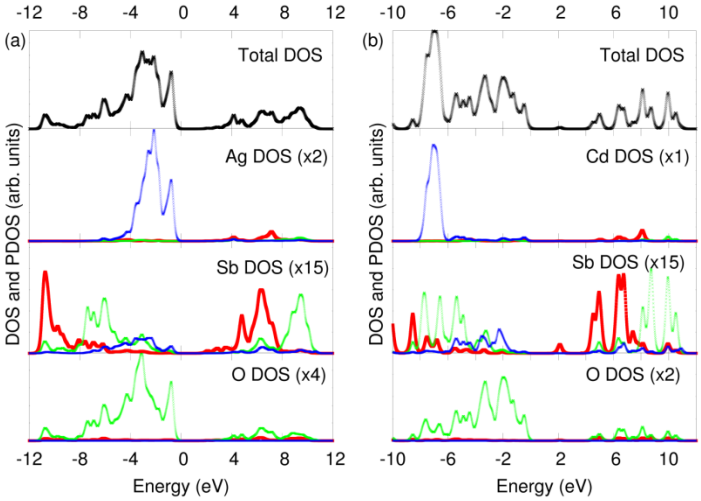
(a)
Total DOS
Ag DOS (x2)
Sb DOS (x15)
O DOS (x4)
DOS and PDOS (arb. units)
-12 -8 -4 0 4 8 12
Energy (eV)
(b)
Total DOS
Cd DOS (x1)
Sb DOS (x15)
O DOS (x2)
DOS and PDOS (arb. units)
-10 -6 -2 2 6 10
Energy (eV)

Figure 8:

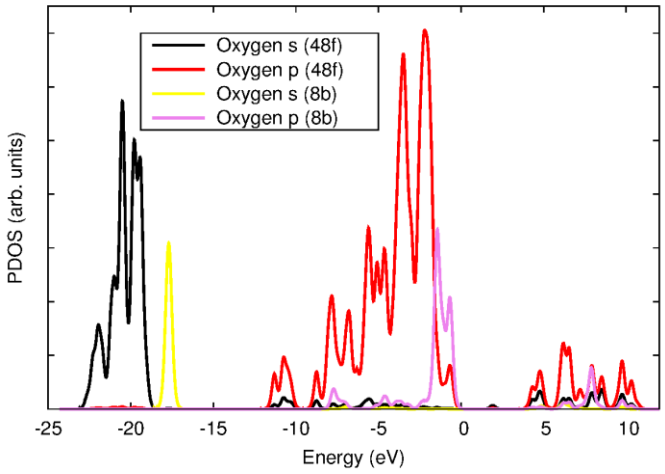
Oxygen s (48f)
Oxygen p (48f)
Oxygen s (8b)
Oxygen p (8b)
PDOS (arb. units)
-25
-20
-15
-10
-5
0
5
10
Energy (eV)

Figure 9.

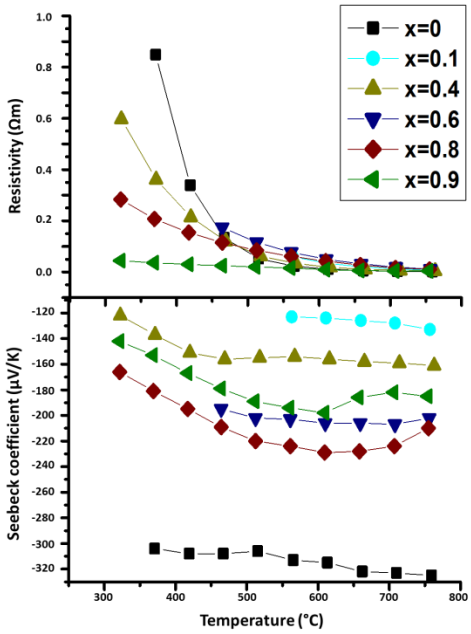
x=0
x=0.1
x=0.4
x=0.6
x=0.8
x=0.9
Resistivity (Ωm)
Seebeck coefficient (μV/K)
Temperature (°C)

Figure 10.

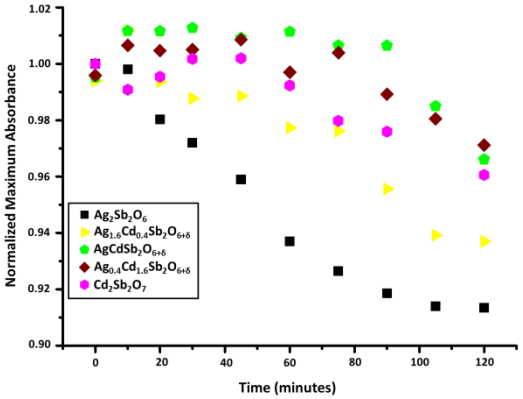
Normalized Maximum Absorbance
Time (minutes)
1.02
1.00
0.98
0.96
0.94
0.92
0.90
0
20
40
60
80
100
120
Ag2Sb2O6
Ag1.6Cd0.4Sb2O6+δ
AgCdSb2O6+δ
Ag0.4Cd1.6Sb2O6+δ
Cd2Sb2O7

Figure 11.

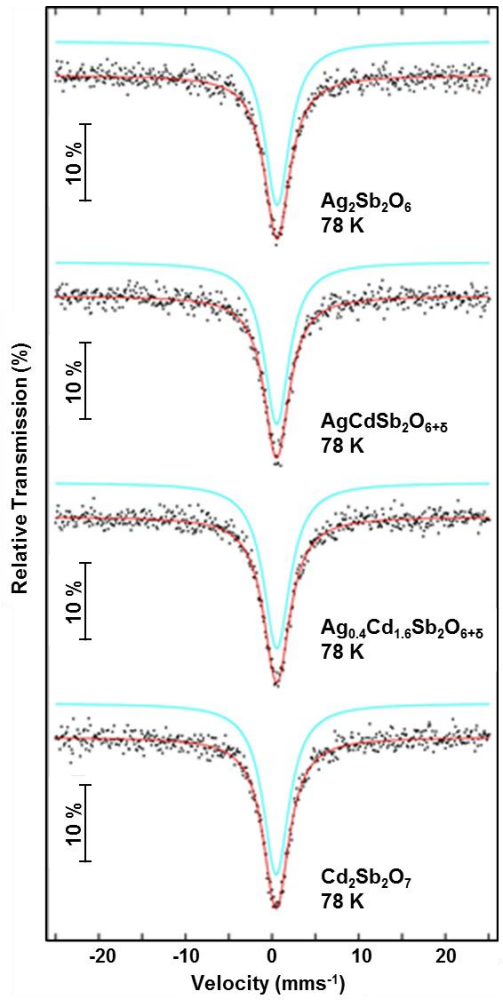
Relative Transmission (%)
10 %
$Ag_2Sb_2O_6$
78 K
10 %
$AgCdSb_2O_{6+\delta}$
78 K
10 %
$Ag_{0.4}Cd_{1.6}Sb_2O_{6+\delta}$
78 K
10 %
$Cd_2Sb_2O_7$
78 K
-20
-10
0
10
20
Velocity (mms^{-1})